The Rotordynamic Forces on a Centrifugal Pump Impeller in the Presence of Cavitation

R. Franz

A. J. Acosta

C. E. Brennen

T. K. Caughey

California Institute of Technology,
Pasadena, CA 91125

An experiment in forced vibration was conducted to study the fluid-induced rotordynamic force on an impeller whirling along a trajectory eccentric to its undeflected position in the presence of cavitation. The prescribed whirl trajectory of the rotor is a circular orbit of a fixed radius. The force measured is a combination of a steady radial force due to volute asymmetries and an unsteady force due to the eccentric motion of the rotor. These measurements have been conducted over a full range of whirl/impeller speed ratios at different flow coefficients without cavitation for various turbomachines. A destabilizing force was observed over a region of positive whirl ratio. The range of flow conditions examined for a centrifugal impeller in a spiral volute has been enlarged to include cavitation. Compared to the non-cavitating condition, cavitation corresponding to a head loss of three percent did not have a significant effect upon the unsteady force. However, a lesser degree of cavitation at the design point increased the destabilizing force for a particular set of whirl ratios.

Introduction

Fluid-induced forces acting on the impeller and therefore on the bearings of a turbomachine can cause self-excited whirl, where the rotor moves away from and whirls along a trajectory eccentric to its undeflected position. Knowledge of the unsteady force related to the lateral vibration of the rotor is crucial to understanding the rotordynamics of the turbomachine. This force has been measured on pump impelleres by various authors: Bolleter et al. (1987), Ohashi and Shoji (1987), Ohashi et al. (1988), Jery et al. (1985), and Jery (1987). Bolleter translated the impeller inside a vaned diffuser along a single axis using a "rocking arm" excited by a transient frequency sweep. The test section was typical of a single stage of a boiler feed pump. Ohashi, using a circular whirl motion, first tested two-dimensional impellers and then employed a rebuilt eccentric whirl mechanism to test a centrifugal impeller in a vaned diffuser. Also, a spacer was inserted to decrease the clearance around the impeller shroud.

This paper presents data taken using the same facility as Jery, who had measured the forces on a five bladed centrifugal impeller (designated Impeller X) in various vaneless and vaned diffusers, among them a spiral volute (Volute A). Adkins (1986) and Adkins and Brennen (1988) observed that the pressure distribution around the front shroud of Impeller X had a significant contribution to the hydrodynamic stiffness. He also reported measurements taken with the annular region surrounding the shroud exposed to the volute housing reservoir. This data was compared with measurements taken without the enlarged annular region surrounding the shroud and with a two dimensional version of the impeller, Franz et al. (1987), demonstrating that the large shroud clearances reduce the magnitude of the rotordynamic forces for reverse whirl and destabilizing forward whirl. Bolleter, who had a smaller gap between the impeller shroud and the casing, measured larger forces. The present investigation extends the range of operating conditions of the centrifugal impeller to include the effect of cavitation.

Experimental Facility

The references (Brennen et al. 1980, Jery 1987 and Franz 1989) provide a description of the Rotor Force Test Facility,

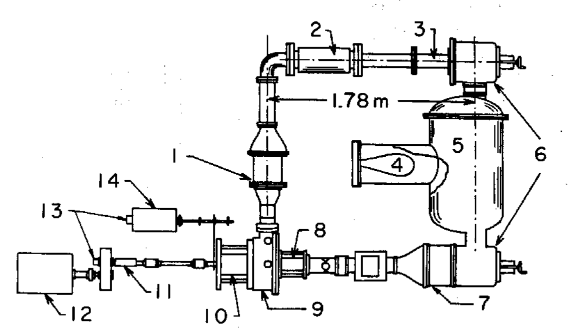

Fig. 1 Layout of the Rotor Force Test Facility. Downstream flow smoothing section (1), "silent" throttle valve (2), turbine flow meter (3), air bladder (4), reservoir, heat exchanger and air removal (5), flow fluctuators (dismantled) (6), upstream flow smoothing section (7), lucite viewing window (8), centrifugal pump test section (9), eccentric drive mechanism (10), slip ring assembly (11), main shaft motor (12), optical encoders (13), whirl motor (14).

Contributed by the Fluids Engineering Division for publication in the Journal of Fluids Engineering. Manuscript received by the Fluids Engineering Division May 15, 1989.

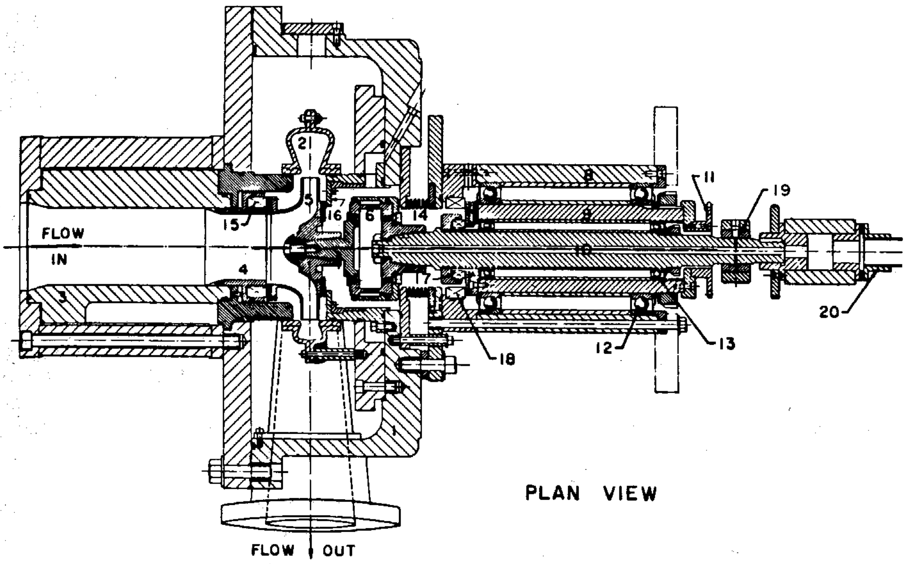

Fig. 2 Assembly drawing of the test section and the eccentric drive mechanism. Pump housing (1), volute (2), inlet connection (3), inlet bell (4), impeller (5), rotating dynamometer (6), eccentric drive mechanism: outer and inner bearing carriers (8 and 9), main shaft (10), orbiting motion sprocket (11), outer and inner bearing sets (12 and 13), bellows (14), impeller front face seal (15), back seal (16), eccentric drive inner and outer face seals (17 and 18), air bearing stator (19), flexible coupling (20).

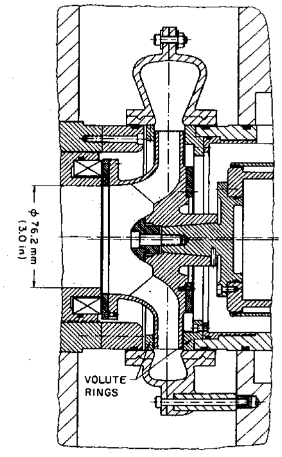

Fig. 3 Assembly drawing of Impeller X and Volute A installed in the test section

a water recirculating pump loop, closed to the atmosphere, Fig. 1. The flow was throttled by the "silent valve" which was comprised of a block of elastomer containing about 200 longitudinal holes that was squeezed axially by a hydraulic cylinder under feedback control to the turbine flow meter. Pressure transducers measured the static pressure after honeycomb screens at the end of the upstream and downstream flow smoothing sections. By altering the absolute pressure of air inside an air bladder in the reservoir, the datum pressure of the pump loop can be controlled, enabling tests in the presence of cavitation. The water had a dissolved air content of 4 ppm and a temperature of 120°F during the tests.

The force measuring device is a rotating dynamometer mounted between the impeller and the main drive shaft. The dynamometer consists of two parallel plates connected by four parallel bars which are strain gaged to measure the six components of force and moment. The strain gages are wired to form Wheatstone bridges. The impeller is made to whirl in a circular orbit eccentric to the volute center of radius $\epsilon = 1.26$ mm (.0495 in.), in addition to the normal shaft rotation, using a double bearing cartridge assembly. Figure 2 shows the test section and the eccentric drive mechanism. For the tests presented the main shaft speed was 2000 rpm. Using optical encoders to provide feedback, each motor was closed-loop controlled to be synchronized with data acquisition. The phase error of each motor was ± 1 degree. Since the eccentric motion is in the lateral plane, perpendicular to the impeller centerline, only the force and moment in this lateral plane will be discussed.

The impeller used, designated Impeller X, was a five bladed, cast bronze impeller, donated by Byron-Jackson of Long Beach, CA. It has a specific speed of .57 and a discharge blade angle of 25 deg with respect to the axizmuthal tangent. The "well-matched" spiral volute of trapezoidal cross section, Volute A, was made of fiberglass. Drawings of the impeller and the volute are accessible in Adkins and Brennen (1988). Figure 3 is an assembly drawing of Impeller X and Volute A installed in the test section. The front face seal had a clearance of .13 mm (.005 in.). To reduce leakage flow from the impeller discharge, rings were installed inside the volute. The front and back volute rings had an axial clearance of .25 mm (.010 in.) and .13 mm (.005 in.), respectively.

Nomenclature

$[A]$ = hydrodynamic force matrix, nondimensionalized by $\frac{1}{2}\rho u_2^2 A_2/r_2$

A_1, A_2 = impeller inlet area (πr_1^2), outlet area ($2\pi r_2 b_2$)

$[B]$ = hydrodynamic moment matrix, nondimensionalized by $\frac{1}{2}\rho u_2^2 A_2$

b_2 = impeller discharge width, 15.7 mm (0.62 in.)

$[C]$ = hydrodynamic damping matrix, nondimensionalized by $\frac{1}{2}\rho u_2^2 A_2/(r_2\omega)$

F_1, F_2 = components of the instantaneous lateral force on the impeller in the rotating dynamometer reference frame

F_x, F_y = components of the instantaneous lateral force on the impeller in the stationary volute frame, nondimensionalized by $\frac{1}{2}\rho u_2^2 A_2$

F_{ox}, F_{oy} = values of F_x and F_y if the impeller was located at the origin of the volute frame, non-dimensionalized by $\frac{1}{2}\rho u_2^2 A_2$

F_n, F_t = components of the lateral force on the impeller which are normal to and tangential to the whirl orbit, averaged over the orbit, nondimensionalized by $\frac{1}{2}\rho u_2^2 A_2 \epsilon/r_2$

$[K]$ = hydrodynamic stiffness matrix, nondimensionalized by $\frac{1}{2}\rho u_2^2 A_2/r_2$

$[M]$ = hydrodynamic mass matrix, nondimensionalized by $\frac{1}{2}\rho u_2^2 A_2/(r_2\omega^2)$

M_x, M_y = components of the instantaneous lateral moment on the impeller in the fixed volute frame, nondimensionlized by $\frac{1}{2}\rho u_2^2 A_2 r_2$

M_{ox}, M_{oy} = values of M_x and M_y if the impeller was located at the origin of the volute frame, nondimensionalized by $\frac{1}{2}\rho u_2^2 A_2 r_2$

M_n, M_t = components of the lateral moment on the impeller which are normal to and tangential to the whirl orbit, averaged over the orbit, nondimensionalized by $\frac{1}{2}\rho u_2^2 A_2 \epsilon$

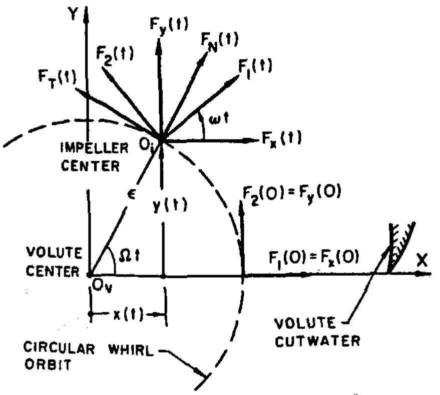

Fig. 4 Schematic representation of the lateral forces on an impeller whirling in a circular orbit. F_1 and F_2 are in the rotating dynamometer frame. F_x and F_y are in the stationary volute frame. F_n and F_t are in the local polar coordinate frame, normal to and tangential to the circular whirl orbit.

Data Processing

Referring to Fig. 4, the forces in the stationary volute frame of reference, assuming a small displacement, can be represented by

$$\mathbf{F}(t) = \mathbf{F}_0 + [\mathbf{A}]\mathbf{x}(t) \tag{1}$$

The lateral force, $\mathbf{F}(t)$, can be considered as the sum of two forces: a steady force, $\mathbf{F}_0$, which the impeller would experience if located at the volute center, and an unsteady force due to the eccentric motion of the impeller, represented by a force matrix $[\mathbf{A}]$; $\mathbf{x}(t)$ is the displacement vector of the impeller from the volute center.

For the forced vibration experiment conducted, the imposed whirl trajectory was a circular orbit of radius ϵ and frequency Ω. The lateral forces detected by the dynamometer in the rotating frame, F_1 and F_2, are related to the lateral forces in the volute frame, F_x and F_y, by a rotation through the angle $-\omega t$, where ω is the frequency of main shaft rotation.

$$\begin{aligned} F_1(t)\cos(\omega t) - F_2(t)\sin(\omega t) &= F_{ox} + \epsilon A_{xx}\cos(\Omega t) + \epsilon A_{xy}\sin(\Omega t) \\ F_1(t)\sin(\omega t) + F_2(t)\cos(\omega t) &= F_{oy} + \epsilon A_{yx}\cos(\Omega t) + \epsilon A_{yy}\sin(\Omega t) \end{aligned} \tag{2}$$

The components of the steady force are obtained by averaging each equation. The elements of the hydrodynamic force matrix: A_{xx}, A_{yx} and A_{xy}, A_{yy} are obtained by evaluating the cos and sin Fourier coefficients, respectively, of each equation.

The unsteady force, $[\mathbf{A}]\epsilon(t)$, due to the eccentric motion of the impeller can be resolved into its components, F_n and F_t, normal to and tangential to the whirl orbit, averaged over the orbit. The normal force is considered positive radially outward. The tangential force is positive when in the direction of the shaft rotation. For the imposed circular whirl orbit

$$\begin{aligned} F_n &= \frac{1}{2}(A_{xx}+A_{yy})\epsilon \\ F_t &= \frac{1}{2}(-A_{xy}+A_{yx})\epsilon \end{aligned} \tag{3}$$

Whenever the tangential force is in the same direction as the whirl motion it encourages the whirl motion and is thus destabilizing. A positive normal force tends to increase the radius of the whirl motion. F_n and F_t are nondimensionalized by the additional factor ϵ/r_2 so that they would be numerically equal to the average of the appropriate matrix elements. The Nomenclature gives the details.

The lateral moment experienced by the whirling impeller can be expressed in the stationary volute frame as

$$\mathbf{M}(t) = \mathbf{M}_0 + [\mathbf{B}]\epsilon(t) \tag{4}$$

The moment is measured in the plane bisecting the impeller discharge area. The expressions for $\mathbf{M}_0$ and $[\mathbf{B}]$ are similar to the force equations. A positive M_t would tend to tilt the impeller outward. M_n with the same sign as the whirl velocity would tend to tilt the impeller inlet away from the whirl direction.

To experimentally extract the fluid-induced forces at a given whirl ratio and operating condition, two identical tests are performed, one in air and the other in water. The forces from the former experiment are subtracted from the latter to yield the fluid-induced forces. The buoyancy force on the rotor is subtracted separately.

For data taken without whirl, the $\Omega/\omega=0$ point, the impeller is placed at four locations on its eccentric orbit, each 90 degrees apart, corresponding to the location nearest the volute tongue, farthest, and the two intermediary locations. The steady force is computed from the average of the main shaft component. The matrix $[\mathbf{A}]$ at $\Omega/\omega=0$, the stiffness matrix, is computed by subtracting the appropriate force components of diametrically opposite whirl orbit locations.

The dynamometer was calibrated statically in situ using an arrangement of cables, pulleys and weights. Its dynamic response was checked by rotating and whirling the impeller in air. The dynamometer measured as periodic forces gravity and the centrifugal force from whirling in a circular orbit. From rotating in air for various shaft speeds up to 3500 rpm, the weight of Impeller X was measured. The magnitude of the

Nomenclature (cont.)

p_1, p_{t1} = upstream static, total pressure
p_2, p_{t2} = downstream static, total pressure
p_I = static pressure at impeller inlet, $p_{t1} - \frac{1}{2}\rho\left(\frac{Q}{A_1}\right)^2$
p_v = vapor pressure of water
Q = flow rate
r_1, r_2 = impeller inlet, discharge radius; 40.5 mm (1.594 in.), 81.0 mm (3.188 in.)
t = time
u_1, u_2 = impeller tip speed at impeller inlet, ωr_1, at discharge, ωr_2
x, y = instantaneous coordinates of the impeller center in the stationary volute frame, nondimensionalized by r_2
z = coordinate of the machine axis, pointing upstream in the direction of impeller rotation from the plane bisecting the impeller outlet area, nondimensionalized by r_2
ϵ = radius of circular whirl orbit, 1.26 mm (.0495 in.)
θ = angular position of the impeller on the whirl orbit, measured from the volute tongue in the direction of impeller rotation
ρ = density of water
σ = cavitation number, $\frac{p_I - p_v}{\frac{1}{2}\rho u_1^2}$
σ^2 = variance
ϕ = flow coefficient, $\frac{Q}{u_2 A_2}$
ψ = total head coefficient, $\frac{p_{t2}-p_{t1}}{\rho u_2^2}$
ω = radian frequency of the impeller (shaft) rotation
Ω = radian frequency of the whirl motion

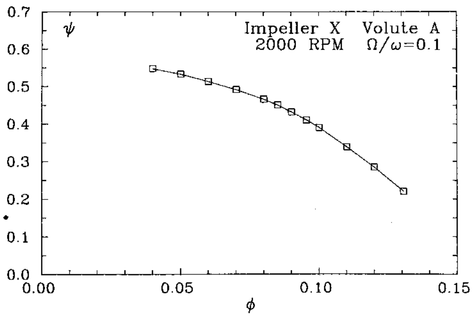

Fig. 5 Noncavitating performance curve of Impeller X in Volute A at 2000 rpm with $\Omega/\omega = .1$. Uncertainty expressed as a standard deviation: $\psi \pm .005$ and $\phi \pm .0005$.

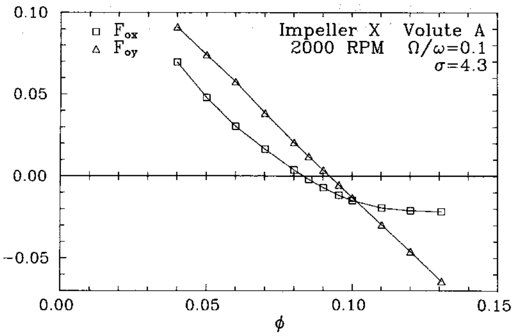

Fig. 6 The components of the steady force F_{ox} and F_{oy}, on Impeller X in Volute A at 2000 rpm as a function of flow coefficient. Uncertainty expressed as a standard devitation: F_{ox}, $F_{oy} \pm .00078$ and $\phi \pm .0005$.

components F_1 and F_2 were within 1 percent and the phase error was less than 1 degree. The phase angle of the forces measured while rotating and whirling in air was used to check the orientation of the optical encoders on the main and whirl shafts, for synchronization with data taking.

The unsymmetric lateral stiffness of the entire structure including the eccentric drive mechanism introduced a resonance into the measurements when observed in the rotating dynamometer frame, F_1 and F_2, due to the observed time dependent stiffness. When transformed into the stationary frame the resonance disappeared from the force components, Franz (1989), and did not affect the data presented.

Presentation of Data

For the present investigation of the rotor forces the phenomenon of cavitation could not be physically observed. Its presence was inferred from pump performance loss and from its influence upon the dynamometer measurements. The impeller force depends upon the location of the impeller within the volute. By whirling the impeller, a single measurement can be used to obtain the steady force. With $\Omega/\omega = .1$, the noncavitating performance and the components of the steady force, F_{ox} and F_{oy}, are plotted against flow coefficient in Figs. 5–6, respectively. In terms of the magnitude and angle of the force vector measured from the volute tongue in the direction of main shaft rotation, the minimum of the steady force and greatest angular change occur at design, $\phi = .092$.

The effect of cavitation upon the hydrodynamic forces was examined by testing three flow coefficients: $\phi = .120$, .092 (design) and .060. The cavitating performance curves are given in Fig. 7. The operating constraint of keeping the pressure of the back seal cavity above atmosphere permitted a breakdown in head rise across the pump of approximately 15, 20, and 25 percent for the flow coefficients $\phi = .120$, .092 (design) and .060, respectively.

The dependence of the magnitude and direction of the steady

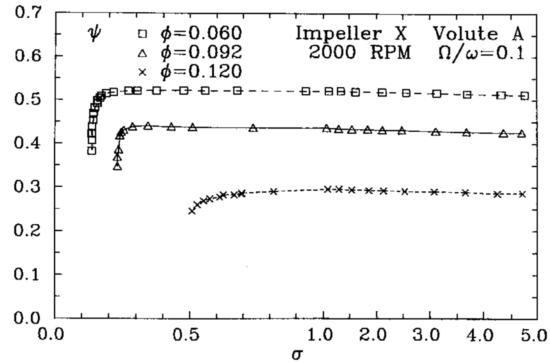

Fig. 7 Cavitation performance curve at 2000 rpm with $\Omega/\omega = .1$ for three flow coefficients: $\phi = .120$, .092 (design) and .060. Uncertainty expressed as a standard deviation: $\psi \pm .005$ and $\sigma \pm .008$.

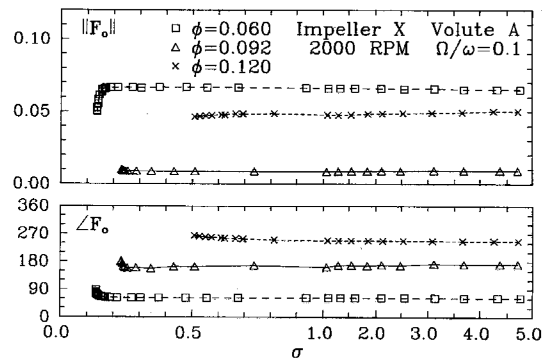

Fig. 8 The magnitude and direction of the steady force $\mathbf{F}_0$ on Impeller X in Volute A at 2000 rpm with $\Omega/\omega = .1$ for the three coefficients: $\phi = .060$, .092 (design) and .120, as a function of the cavitation number. Uncertainty expressed as a standard deviation: $\|\mathbf{F}_0\| \pm .00078$, $\angle \mathbf{F}_0 \pm 1$ deg (5 deg for $\phi = .092$).

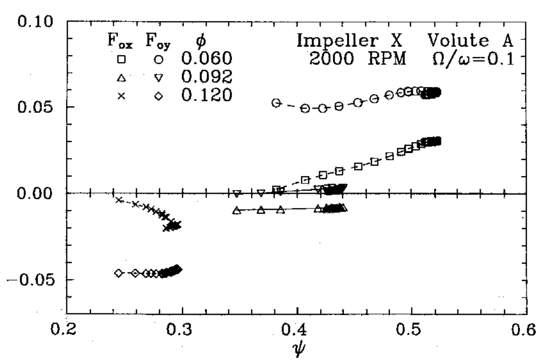

Fig. 9 The components of the steady force, F_{ox} and F_{oy}, on Impeller X in Volute A at 2000 rpm with $\Omega/\omega = .1$ for the three flow coefficients: $\phi = .060$, .092 (design) and .120, as a function of the head coefficient. Uncertainty expressed as a standard deviation: F_{ox}, $F_{ox} \pm .00078$ and $\psi \pm .005$.

force upon cavitation number is shown in Fig. 8. For off-design, $\phi = .120$ and $\phi = .060$, the magnitude of $\mathbf{F}_0$ decreases with breakdown. For design the magnitude of $\mathbf{F}_0$ decreases with decreasing cavitation number until the knee of the performance curve. It increases above the noncavitating value in breakdown. It varied less than 10 percent from the noncavitating value. The direction of $\mathbf{F}_0$ rotates away from the tongue in the direction of impeller shaft rotation for each flow coefficient through breakdown.

The components of $\mathbf{F}_0$ in the volute reference frame are plotted against head coefficient in Fig. 9. From preliminary data taken at 3000 rpm, Fig. 10 shows the steady force components for various flow coefficients at the operating points: noncavitating, 3 percent head loss and 10 percent head loss.

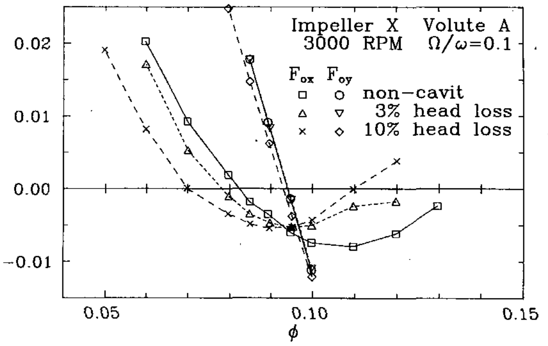

Fig. 10 The components of the steady force, F_{ox} and F_{ox}, on Impeller X in Volute A at 3000 rpm with $\Omega/\omega = .1$ for the three operating conditions: non-cavitating, 3 percent head loss and 10 percent head loss as a function of the flow coefficient focusing upon design. Uncertainty expressed as a standard deviation: F_{ox}, $F_{oy} \pm .00078$ and $\phi \pm .0005$.

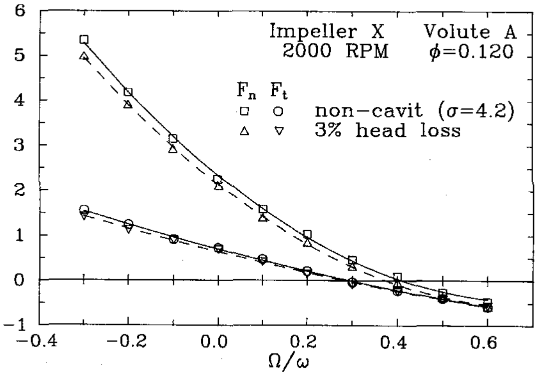

Fig. 11 The average normal and tangential force, F_n and F_t, on Impeller X in Volute A at 2000 rpm at a flow coefficient of $\phi = .120$ as a function of whirl ratio for flow without cavitation and with a head loss of 3 percent. Uncertainty expressed as a standard deviation: $F_n \pm .04$, $F_t \pm .047$ and $\Omega/\omega \pm .001$.

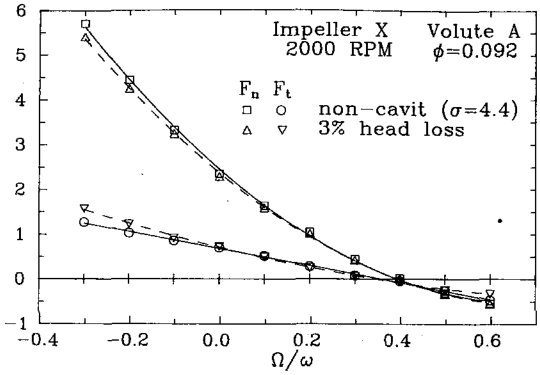

Fig. 12 The average normal and tangential force, F_n and F_t, on Impeller X in Volute A at 2000 rpm at design flow ($\phi = .092$) as a function of whirl ratio for flow without cavitation and with a head loss of 3 percent. Uncertainty expressed as a standard deviation: $F_n \pm .04$, $F_t \pm .047$ and $\Omega/\omega \pm .001$.

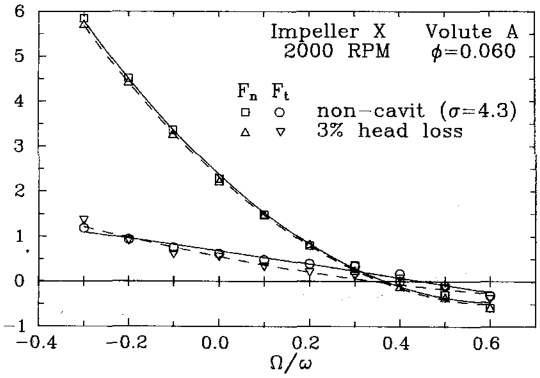

Fig. 13 The average normal and tangential force, F_n and F_t, on Impeller X in Volute A at 2000 rpm at a flow coefficient of $\phi = .060$ as a function of whirl ratio for flow without cavitation and with a head loss of 3 percent. Uncertainty expressed as a standard deviation: $F_n \pm .04$, $F_t \pm .047$ and $\Omega/\omega \pm .001$.

The setup was slightly different, so this figure should not be directly compared with the other data presented. The steady force component in the direction of the volute tongue, F_{ox}, was affected more by cavitation. With increasing head loss, the curve F_{ox} as a function of ϕ appears to rotate about design flow. For a centrifugal impeller in a volute pump tested at several flow coefficients above best efficiency, Uchida et al. (1971) had also observed that the steady force component in the tongue direction increases with developing cavitation.

For each flow coefficient measurements were taken over the whirl ratio range $-.3 \le \Omega/\omega \le .6$ in increments of .1 at two cavitation numbers: one non-cavitating and the other corresponding to a head loss of 3 percent. The normal and tangential forces as a function of whirl ratio are plotted in Figs. 11–13. For these figures the drawn curves are a quadratic fit to the data. Over a range of forward whirl F_t is in the same direction as the whirl motion, thus destabilizing. By $\Omega/\omega = .6$, the tangential force had become stabilizing again, consequently tests at higher whirl ratios were not necessary. At 3 percent head loss, F_n is slightly smaller and the magnitude of F_t is smaller for positive Ω/ω. At $\Omega/\omega = -.3$, $\phi = .120$, F_t is smaller; though for $\phi = .092$ (design) and $\phi = .060$, F_t is larger than for the non-cavitating case. The range of destabilizing forward whirl ratio was slightly reduced by cavitation at 3 percent head loss. For forward whirl there is a region over which $F_n < 0$, and tends to decrease the whirl radius. Based on past experiments, F_n will be positive again at higher whirl ratios, reflecting its parabolic character. At design, $\phi = .092$, the zero-crossing whirl ratios for F_n and F_t are nearly the same. F_t is destabilizing over the same range of whirl ratio as F_n tends to increase the whirl orbit radius. For $\phi = .060$, F_t is positive up to a higher Ω/ω, whereas for $\phi = .120$, the destabilizing region is smaller than the region over which F_n would increase the whirl radius. The region of destabilizing whirl ratio decreases with increasing flow coefficient.

For two whirl ratios in the region of destabilizing whirl, $\Omega/\omega = .1$ and .3, measurements were taken from non-cavitating conditions through breakdown of the head rise across the pump. Each set of the breakdown measurements was done in a single sitting. The steady force from $\Omega/\omega = .1$ has already been presented. The effect of cavitation upon the steady force components F_n and F_t is shown in Figs. 14–15. For the above design flow coefficient, $\phi = .120$, they decrease with head loss. For $\Omega/\omega = .3$, F_t becomes slightly more negative, increasing the stability margin.

At design flow, $\phi = .092$, for $\Omega/\omega = .1$, F_n and F_t decrease with head loss, however, for a head loss greater than 10 percent there is a slight rise in F_t. The data for $\Omega/\omega = .3$ exhibit similar behavior except in the region between the peak head rise and 1 percent head loss, where F_n goes through a trough and F_t a peak. Through this swing the unsteady force increases slightly in magnitude and rotates in a direction to increase the destabilizing tangential force, then rotates back. Evident from the later Fig. 21, both M_n and M_t increase in this region before decreasing with head loss. The unsteady moment vector swings only a few degrees in the direction to increase M_n. Figure 16 shows that this perturbation is reflected in the steady force calculated from the $\Omega/\omega = .3$ data, which swings in the direction of main shaft rotation. For this operating region the flow was sufficiently disturbed so that the linearization of $\mathbf{F}(t)$, equation (1), which represents the unsteady force by $[\mathbf{A}]\epsilon(t)$, is invalid; since for $\Omega/\omega = .3$, $\mathbf{F}_0$ was perturbed.

For below design flow, $\phi = .060$, F_n and F_t decrease with

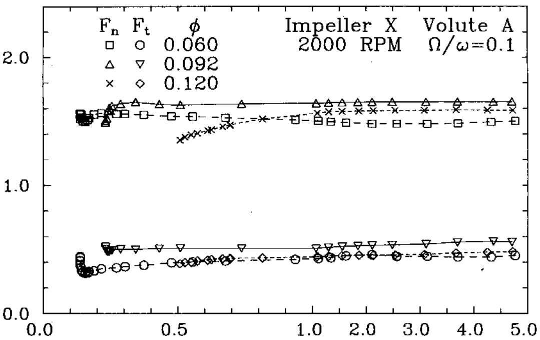

Fig. 14(*a*)

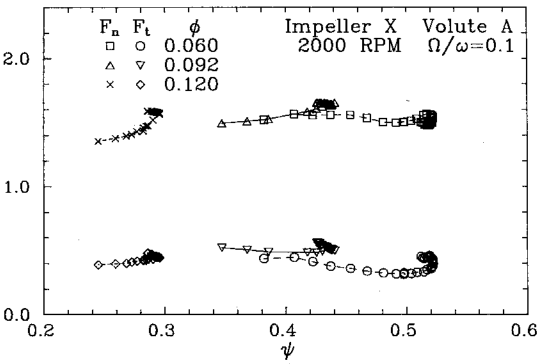

Fig. 14(*b*)

Fig. 14 The average normal and tangential force, F_n and F_t, on Impeller X in Volute A at 2000 rpm with $\Omega/\omega=.1$ for the three flow coefficients: $\phi=.060$, .092 (design) and .120, as a function of (*a*) the cavitation number and (*b*) the head coefficient. Uncertainty expressed as a standard deviation: $F_n \pm .04$, $F_t \pm .047$, $\sigma \pm .008$ and $\psi \pm .005$.

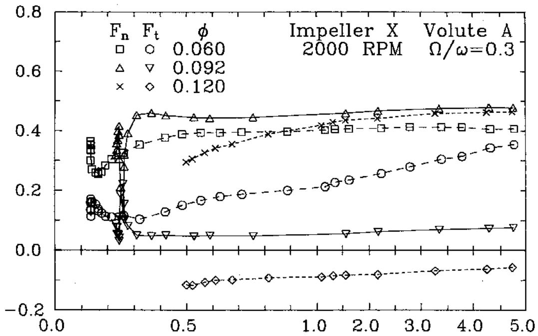

Fig. 15(*a*)

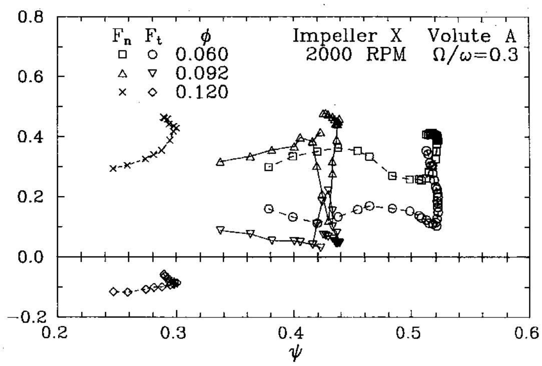

Fig. 15(*b*)

Fig. 15 The average normal and tangential force, F_n and F_t, on Impeller X in Volute A at 2000 rpm with $\Omega/\omega=.3$ for the three flow coefficients: $\phi=.060$, .092 (design) and .120, as a function of (*a*) the cavitation number and (*b*) the head coefficient. Uncertainty expressed as a standard deviation: $F_n \pm .04$, $F_t \pm .047$, $\sigma \pm .008$ and $\psi \pm .005$.

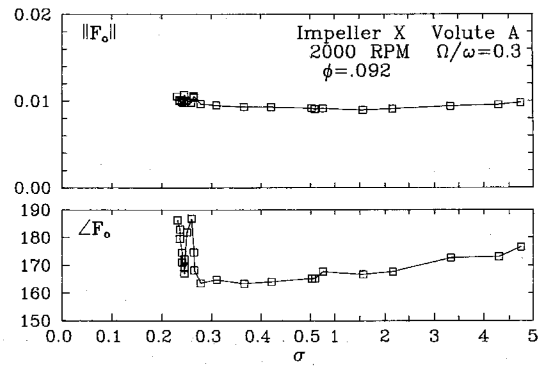

Fig. 16 The magnitude and direction of the steady force $\mathbf{F}_0$ on Impeller X in Volute A at 2000 rpm with $\Omega/\omega=.3$ at design flow ($\phi=.092$) as a function of the cavitation number. Uncertainty expressed as a standard deviation: $\|\mathbf{F}_0\| \pm .00078$, $\angle\, \mathbf{F}_0 \pm 5$ deg.

developing cavitation. For $\Omega/\omega=.1$, though, F_n increases approaching the knee before decreasing with breakdown, while F_t increases with loss. For $\Omega/\omega=.3$, F_n decreases with breakdown though momentarily increasing with head loss. F_t, doing the opposite, increases with breakdown.

Data were taken over 256 cycles of the reference frequency ω/J (where $\Omega/\omega=I/J$, I, J integers) at which the orientation of the dynamometer and its location on the whirl orbit geometrically repeat. For each cycle $\mathbf{F}_0$ and $[\mathbf{A}]$ were computed. The variances, over the 256 cycles, including the tests performed in air, were calculated for $\Omega/\omega=-.1$, .1, .3 and .5, from the whirl ratio sets and for selected runs of the breakdown sets. The standard deviations were typically less than .00078 for F_{ox} and F_{oy}, .04 for F_n and .047 for F_t. For $\Omega/\omega=.5$ the standard deviations were occasionally larger than the mentioned values. For the breakdown sets of $\Omega/\omega=.3$, frequently the small values of F_t were not significantly larger than the associated standard deviations.

Discussion of Moments

The lateral moments of the whirling impeller are measured in the calibration plane of the dynamometer which coincides with the plane bisecting the discharge area of the impeller. With primary interest in the unsteady rotor forces which can encourage self-excited whirl, attention will be focused on the unsteady moments.

For the three flow coefficients tested Figs. 17–19 present M_n and M_t as a function of whirl ratio for the two operating conditions: noncavitating and 3 percent head loss. M_t is positive, tending to tilt the impeller outward. The magnitude increases with increasing positive whirl ratio. The values are larger for lower flow coefficients. M_n is in the same direction as the whirl velocity, except in the region where the value is small for small whirl ratios. M_n resembles a cubic function of Ω/ω. From data taken in the past with non-cavitating flow, for higher reverse whirl ratios M_t increases and M_n decreases.

To obtain lever arms the relation $\mathbf{r}\times\mathbf{F}=\mathbf{M}$ is used with the assumption that the axial thrust acts along the impeller centerline. To simplify the discussion, the contribution of the unsteady lateral force to the moment from the external shroud and the impeller blades will be considered.

$$\begin{aligned} M_n &= -z_{\text{shroud}}F_{t,\text{shroud}} - z_{\text{blade}}F_{t,\text{blade}} \\ M_t &= z_{\text{shroud}}F_{n,\text{shroud}} + z_{\text{blade}}F_{n,\text{blade}} \end{aligned} \tag{5}$$

where the z axis points upstream. Unless the forces $\mathbf{F}_{\text{shroud}}$ and $\mathbf{F}_{\text{blade}}$ are parallel the introduced moment will not be perpendicular to $\mathbf{F}$, and $M_t/F_n \neq -M_n/F_t$.

The lever arms computed from $z=M_t/F_n$ and $-M_n/F_t$ depend significantly upon whirl ratio in the region of forward

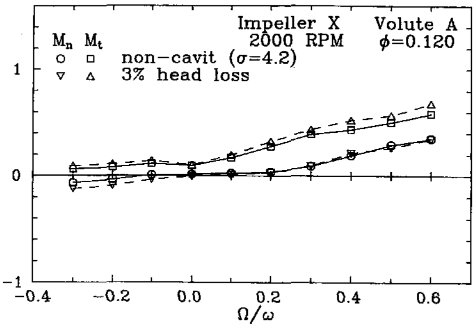

Fig. 17 The average normal and tangential moment, M_n and M_t, on Impeller X in Volute A at 2000 rpm at a flow coefficient of $\phi = .120$ as a function of whirl ratio for flow without cavitation and with a head loss of 3 percent. Uncertainty expressed as a standard deviation: M_n, $M_t \pm .11$ and $\Omega/\omega \pm .001$.

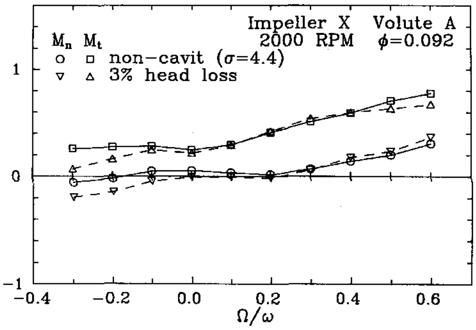

Fig. 18 The average normal and tangential moment, M_n and M_t, on Impeller X in Volute A at 2000 rpm at design flow ($\phi = .092$) as a function of whirl ratio for flow without cavitation and with a head loss of 3 percent. Uncertainty expressed as a standard deviation: M_n, $M_t \pm .11$ and $\Omega/\omega \pm .001$.

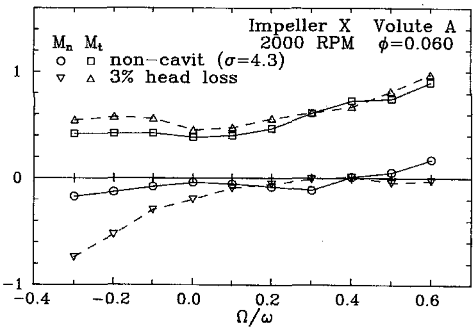

Fig. 19 The average normal and tangential moment, M_n and M_t, on Impeller X in Volute A at 2000 rpm at a flow coefficient of $\phi = .060$ as a function of whirl ratio for flow without cavitation and with a head loss of 3 percent. Uncertainty expressed as a standard deviation: M_n, $M_t \pm .11$ and $\Omega/\omega \pm .001$.

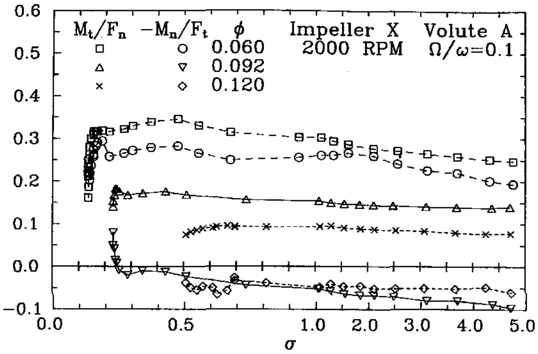

Fig. 20(a)

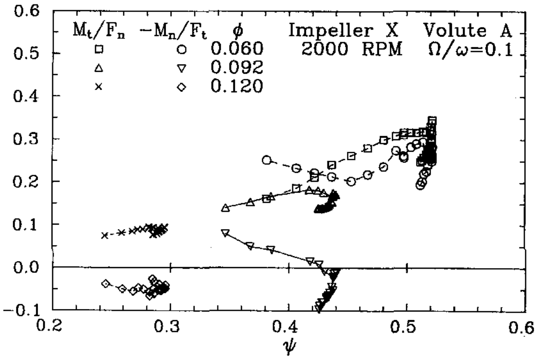

Fig. 20(b)

Fig. 20 The lever arms computed from the components of the unsteady moment and force on Impeller X in Volute A at 2000 rpm with $\Omega/\omega = .1$ for the three flow coefficients: $\phi = .060$, $.092$ (design) and $.120$, as a function of (a) the cavitation number and (b) the head coefficient. Uncertainty expressed as a standard deviation: M_t/F_n, M_n/F_t see text, $\sigma \pm .008$ and $\psi \pm .005$.

where F_n and F_t equal zero. For reverse whirl there is little change. For the breakdown tests taken with $\Omega/\omega = .1$ and $.3$, Figs. 20–21 present the lever arms as an alternative to the moments themselves. Since the measurements are integrated over the entire impeller, the contribution to the moment from each force element of the preceding paragraph is impossible to quantify.

During the course of the experiments, the rotordynamic forces were of primary interest. The moments were obtained during subsequent processing of the data. Fewer sets of instantaneous data were available to compute the variance of [**B**]. Evaluation of the data indicates that the standard deviations were typically less than .11 for M_n and M_t. For many of the whirl ratios presented, the mean of the unsteady moments is not large compared to the scatter over the 256 cycles of a single test. The error in the lever arms was computed using "root-sum-square" for the propagation of uncertainty. The variance of a function f of n independent variables x_i, $i = 1, n$, is $\sigma_f^2 = \sum_{i,j=1}^{n} \frac{\partial f}{\partial x_i}\frac{\partial f}{\partial x_j}\sigma^2_{x_i x_j}$. The error depends upon the magnitude of the denominator, F_n or F_t. For example, at noncavitating design flow the standard deviation of $-M_n/F_t$ for $\Omega/\omega = .1$ and $.3$ is approximately .09 and .5, respectively.

Rotordynamic Force Matrices

The mass-damping-stiffness model of the hydrodynamic force gives,

$$\mathbf{F}(t) = \mathbf{F}_0 - [\mathbf{K}]\mathbf{x}(t) - [\mathbf{C}]\dot{\mathbf{x}}(t) - [\mathbf{M}]\ddot{\mathbf{x}}(t) \tag{6}$$

For the imposed circular whirl orbit, the mass-damping-stiffness model implies that the matrix $[\mathbf{A}(\Omega/\omega)]$ is quadratic in Ω/ω. Since $[\mathbf{A}(\Omega/\omega)]$ does resemble a parabola for the impeller-volute combination presented, the coefficient matrices from a least squares fit are given in Table 1. For the set of Ω/ω tested, the curves A_{xy} and A_{yx} do not quite resemble a parabola for every flow condition. Figure 13 shows that F_t can flatten over the destabilizing whirl ratio range. The standard deviation in the coefficients is approximately .02, .08, and .2 for the stiffness, damping and mass matrices, respectively. For $\phi = .060$, they are larger, in particular .1 for the damping matrix. Over the whirl ratio range tested, the unsteady moments due to the imposed lateral displacement do not in general resemble a quadratic in Ω/ω. Consequently, the coefficients of a quadratic fit are not presented. A complete rotor dynamic analysis would require forces and moments for the deflection as well as the lateral rotation of the rotor about its undeflected position within the volute.

The coefficient matrices presented are for two operating

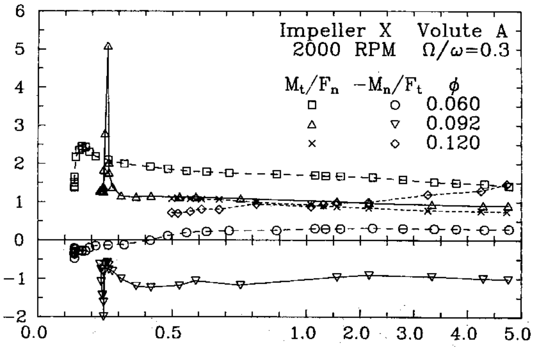

Fig. 21(*a*)

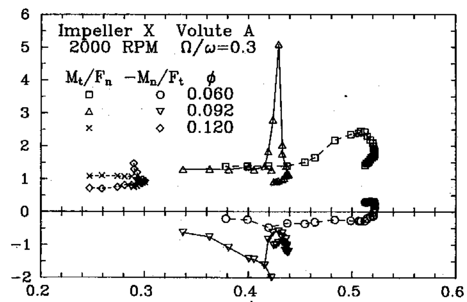

Fig. 21(*b*)

Fig. 21 The lever arms computed from the components of the unsteady moment and force on Impeller X in Volute A at 2000 rpm with $\Omega/\omega = .3$ for the three flow coefficients: $\phi = .060$, .092 (design) and .120, as a function of (*a*) the cavitation number and (*b*) the head coefficient. Uncertainty expressed as a standard deviation: M_t/F_n, M_n/F_t see text, $\sigma \pm .008$ and $\psi \pm .005$.

points: non-cavitating and cavitating with 3 percent head loss. Cavitation at 3 percent head loss did not make the rotor dynamic behavior of the impeller worse. The range of destabilizing whirl ratio was slightly reduced. A monotonic change in the coefficients between the two operating points cannot be assumed. At design flow [A] changes differently for $\Omega/\omega = .1$ and .3 with less cavitation.

Conclusion

Fluid-induced rotordynamic forces were measured in the presence of cavitation for a centrifugal impeller in a spiral volute. At 3 percent head loss there was little difference in the average normal and tangential force, F_n and F_t, for forward whirl, slightly more for the larger values of reverse whirl. The whirl ratio range of the destabilizing force had decreased slightly with cavitation. However a lesser degree of cavitation at the design point increased this destabilizing force for a particular set of whirl ratios. Through breakdown in head rise the destabilizing forces did not exceed their noncavitating values except for this one set of data.

Measurements of the rotordynamic forces on impellers made using the dynamometer of the Rotor Force Test Facility at Caltech are integrated measurements. The contribution to the total force from the varying clearance between the impeller front shroud and the casing wall during whirl is not distinguished from the contribution from the unsteady flow field between the whirling impeller and the volute. Further work is necessary to quantify the contribution of the shroud flow to the impeller force measurements. Childs (1989) has theoretically examined the forces on an impeller shroud. For the impeller-volute interaction Tsujimoto et al. (1988) includes a favorable comparison of his theory with measurements made on a two-dimensional version of Impeller X.

Table 1 Stiffness, damping, and mass matrices. Uncertainty expressed as a standard deviation: $K \pm .02$, $C \pm .08$ and $M \pm .2$. For $\phi = .060$, see text.

flow condition	K_{xx} / K_{yx}	K_{xy} / K_{yy}	C_{xx} / C_{yx}	C_{xy} / C_{yy}	M_{xx} / M_{yx}	M_{xy} / M_{yy}
ϕ=.120	-2.34	.68	2.46	8.19	5.7	-1.2
non-cavit	-.70	-2.34	-7.96	2.70	.3	5.9
ϕ=.120	-2.15	.65	2.27	7.80	5.4	-.9
3% head loss	-.62	-2.12	-7.70	2.58	.4	5.6
ϕ=.092	-2.51	.58	1.88	8.76	6.1	-.4
non-cavit	-.78	-2.38	-8.66	1.92	-.3	6.6
ϕ=.092	-2.42	.60	2.47	8.39	5.6	-1.6
3% head loss	-.81	-2.30	-8.16	2.46	.9	6.0
ϕ=.060	-2.54	.50	1.6	9.2	7.1	-.3
non-cavit	-.84	-2.20	-9.2	1.3	-.6	7.8
ϕ=.060	-2.46	.43	2.0	8.9	6.7	-.9
3% head loss	-.67	-2.17	-9.2	1.8	1.0	7.9

Acknowledgments

The authors are indebted to the NASA George Marshall Space Flight Center, for continued sponsorship of this research under contract NAS8-33108. One of the authors (R. Franz) would like to thank the Shell Foundation for providing a fellowship that sponsored his graduate studies.

References

Adkins, D. R., 1986, "Analyses of Hydrodynamic Forces on Centrifugal Pump Impellers," Ph.D. thesis, Division of Engineering and Applied Science, California Institute of Technology, Pasadena, CA.

Adkins, D. R., Brennen, C. E., 1988, "Analyses of Hydrodynamic Radial Forces on Centrifugal Pump Impellers," ASME JOURNAL OF FLUIDS ENGINEERING, Vol. 110, No. 1, pp. 20–28.

Bolleter, U,. Wyss, A., Welte, I., and Stürchler, R., 1987, "Measurement of Hydrodynamic Interaction Matrices of Boiler Feed Pump Impellers," ASME *Journal of Vibration, Acoustics, Stress, and Reliability in Design*, Vol. 109, No. 2, pp. 144–151.

Brennen, C. E., Acosta, A. J., and Caughy, T. K., 1980, "A Test Program to Measure Fluid Mechanical Whirl-Excitation Forces in Centrifugal Pumps," *Proceedings of the First Workshop on Rotordynamic Instability Problems in High-Performance Turbomachinery*, Texas A&M University, College Station, Texas, NASA CP 2133, pp. 229–235.

Childs, D. W., 1989, "Fluid-Structure Interaction Forces at Pump-Impeller-Shroud Surfaces for Rotordynamic Calculations," ASME *Journal of Vibration, Acoustics, Stress and Reliability in Design*, Vol. 111, No. 3, pp. 216–225.

Franz, R., Arndt, N., Caughey, T. K., Brennen, C. E., and Acosta, A. J., 1987, "Rotordynamic Forces on Centrifugal Pump Impellers," *Proceedings of the Eighth Conference of Fluid Machinery*, Académiai Kiadó, Budapest, Hungary, Vol. 1, pp. 252–258.

Franz, R., 1989, "Experimental Investigation of the Effect of Cavitation on the Rotordynamic Forces on a Whirling Centrifugal Pump Impeller," Ph.D. thesis, Division of Engineering and Applied Science, California Institute of Technology, Pasadena, CA.

Jery, B., Brennen, C. E., Caughey, T. K., and Acosta, A. J., 1985, "Forces on Centrifugal Pump Impellers," *Second International Pump Symposium*, Houston, Texas, Apr. 29–May 2, 1985.

Jery, B., 1987, "Experimental Study of Unsteady Hydrodynamic Force Matrices on Whirling Centrifugal Pump Impellers," Ph.D. thesis, Division of Engineering and Applied Science, California Institute of Technology, Pasadena, CA.

Ohashi, H., Shoji, H., 1987, "Lateral Fluid Forces on a Whirling Centrifugal Impeller (2nd Report: Experiment in Vaneless Diffuser)," ASME JOURNAL OF FLUIDS ENGINEERING, Vol. 109, No. 2, pp. 100–106.

Ohashi, H., Sakurai, A., and Nishihama, J., 1988, "Influence of Impeller and Diffuser Geometries on the Lateral Forces of Whirling Centrifugal Impeller," *Proceedings of the Fifth Workshop on Rotordynamic Instability Problems in High-Performance Turbomachinery*, Texas A&M University, College Station, Texas, May 16–18, 1988.

Tsujimoto, Y., Acosta, A. J., and Brennen, C. E., 1988, "Theoretical Study of Fluid Forces on a Centrifugal Impeller Rotating and Whirling in a Volute," ASME *Journal of Vibration, Acoustics, Stress and Reliability in Design*, Vol. 110, No. 3, pp. 263–269.

Uchida, N., Imaichi, K., and Shirai, T., 1971, "Radial Force on the Impeller of a Centrifugal Pump," *Bulletin of the Japan Society of Mechanical Engineers*, Vol. 14, No. 76, pp. 1106–1117.